

YALE PEABODY MUSEUM

P.O. BOX 208118 | NEW HAVEN CT 06520-8118 USA | PEABODY.YALE. EDU

JOURNAL OF MARINE RESEARCH

The *Journal of Marine Research*, one of the oldest journals in American marine science, published important peer-reviewed original research on a broad array of topics in physical, biological, and chemical oceanography vital to the academic oceanographic community in the long and rich tradition of the Sears Foundation for Marine Research at Yale University.

An archive of all issues from 1937 to 2021 (Volume 1–79) are available through EliScholar, a digital platform for scholarly publishing provided by Yale University Library at <https://elischolar.library.yale.edu/>.

Requests for permission to clear rights for use of this content should be directed to the authors, their estates, or other representatives. The *Journal of Marine Research* has no contact information beyond the affiliations listed in the published articles. We ask that you provide attribution to the *Journal of Marine Research*.

Yale University provides access to these materials for educational and research purposes only. Copyright or other proprietary rights to content contained in this document may be held by individuals or entities other than, or in addition to, Yale University. You are solely responsible for determining the ownership of the copyright, and for obtaining permission for your intended use. Yale University makes no warranty that your distribution, reproduction, or other use of these materials will not infringe the rights of third parties.



This work is licensed under a Creative Commons Attribution-NonCommercial-ShareAlike 4.0 International License.
<https://creativecommons.org/licenses/by-nc-sa/4.0/>



Detailed internal wave mixing above a deep-ocean slope

by Hans van Haren¹ and Louis Gostiaux²

ABSTRACT

Turbulent vertical eddy diffusivity (K_z) and dissipation rate (ϵ) are estimated between 0.5 and 50 m above the sloping side of Great Meteor Seamount, Canary Basin, using 101 moored temperature sensors, 1-mK precision, sampling at 1 Hz. Effectively, detailed observed time-depth temperature images are split in two: a statically stable and a turbulence image. Tides dominate the temperature variations, but the local bottom slope is supercritical to motions at semidiurnal frequencies. Averaged over a fortnight, the observed overall time-depth mean $K_z = 3 \pm 1 \times 10^{-3} \text{ m}^2 \text{ s}^{-1}$ and $\epsilon = 1.5 \pm 0.7 \times 10^{-7} \text{ W kg}^{-1}$. Variations with time and depth are large, by up to four orders of magnitude. Although variations do occur having tidal periodicity, shorter-scale variations are more intense. A particular tidal period shows multiple vigorous overturning events, the largest found away from the bottom during the downslope phase but just prior to arrival of an upslope moving, equally vigorous bore. The strength of the bore may be controlled by the intensity of the mixing just prior to it. The bore itself is turbulent from the bottom upward, up to some 40 m above it. Its mixing is most efficient providing large fluxes in extremely thin layers. Parameterizations of turbulence estimates are inconclusive using powers of N , as they show different relationships for different depths, time-ranges and averaging.

1. Introduction

The ocean, despite being stably stratified in density from surface to bottom, also supports substantial turbulent mixing. This mixing is thought to be mainly induced by dominant motions due to internal waves, and focus is set to most energetic tidal motions (e.g., Munk and Wunsch, 1998). Since internal tides are mainly generated via sloping under water topography, it is conjectured that most mixing occurs above topography rather than in the interior (Munk, 1966; Armi, 1978; Thorpe, 1987; Garrett, 1990). If such mixing is efficient and vigorous enough, it may be sufficient to supply the basin-wide vertical turbulent diffusivity, presently rated at $10^{-4} \text{ m}^2 \text{ s}^{-1}$ (Munk and Wunsch, 1998).

Turbulent, rotationally (Ekman) modified boundary layers are markedly different above sloping topography compared to flat bottoms, with a strong asymmetry for upward and downward steady flows (Weatherly and Martin, 1978; Trowbridge and Lentz, 1991). If time dependence is introduced, the bottom boundary layer above sloping topography may develop

1. NIOZ Royal Netherlands Institute for Sea Research, P. O. Box 59, 1790 AB Den Burg, The Netherlands.
email: hans.van.haren@nioz.nl

2. CNRS/Grenoble-INP/UJF-Grenoble 1, LEGI UMR5519, Grenoble, F-38041, France.

a secondary cross-slope flow (Phillips *et al.*, 1986; Thorpe, 1987), with an alongslope flow as part of the solution (Thorpe, 1987; Garrett, 1990). Sloping topography dynamics also yield a tertiary flow, which expulses mixed waters into the interior (Garrett, 1991). An important feature of such sloping bottom boundary layers is their mixing efficiency: after all, once established homogeneous waters do not mix (anymore). This problem has been elaborated by Garrett (1990).

The solution to the problem of sloping boundary mixing efficiency is a mechanism to rapidly re-stratify the area where mixing takes place. This is potentially achieved by motions that vary on a much smaller time scale than the ones governing the bottom boundary layer, for example internal wave motions. However, when such motions are dominant, as can be the case for internal tides, this may result in completely different bottom boundary layers than for steady flows. Observations have shown that stratification can reach all the way to the sloping bottom with tidal periodicity (van Haren, 2005). This potentially allows for efficient boundary mixing, but further observations have shown that besides stratification also estimates of turbulence parameters vary on a tidal scale above sloping topography (Levine and Boyd, 2006; Aucan *et al.*, 2006; Nash *et al.*, 2007; Aucan and Merrifield, 2008; Klymak *et al.*, 2008). Dissipation rates and eddy diffusivities are reported to vary by a factor of 100, but in contrast with current and temperature records long-term time series do not show a clear spring-neap cycle (Aucan *et al.*, 2006; Klymak *et al.*, 2008).

Here we demonstrate that internal wave motions above sloping topography are completely different from those in the ocean interior: they are not smoothly varying sinusoidal, but nonlinearly varying at all scales, including regular small- and large-scale turbulent overturning. High-resolution moored temperature sensors are used to compute overturns and diverse turbulence parameters in great detail.

2. Data and background

A total of 101 ‘NIOZ3’ temperature sensors sampling at 1 Hz, with precision better than 0.001°C (van Haren *et al.*, 2009), have been deployed at 0.5 m vertical intervals attached to a bottom lander frame. The lowest sensor was nominally at 0.5 m from the bottom. Three sensors failed. Above the thermistor string an acoustic current meter was attached. Its sensors for tilt, heading and pressure showed that the top of the mooring moved <0.15 m vertically and <3.5 m horizontally, thus providing nearly perfect Eulerian measurements. The lander was moored at $30^{\circ} 00.052' \text{N}$, $28^{\circ} 18.802' \text{W}$, $H = 549$ m water depth, near the top of the eastern slope of Great Meteor Seamount (GMS) for 18 days in May/June 2006. The local bottom slope was $4 \pm 1^{\circ}$, confirmed by tilt meter data. The slope was globally orientated ENE as estimated from bathymetry and echosounder data (Fig. 1). The main lunar semidiurnal tidal ellipse has an aspect ratio of 0.8, a major axis amplitude of 0.12 m s^{-1} with orientation NE-SW. Some additional CTD-lowered Acoustic Doppler Current Profiler (LADCP) data were collected around GMS and near the mooring.

The area around the depth of the mooring is stable to double-diffusion, not affected by Mediterranean outflow which is found at least 500 m deeper. Around the mooring depth,

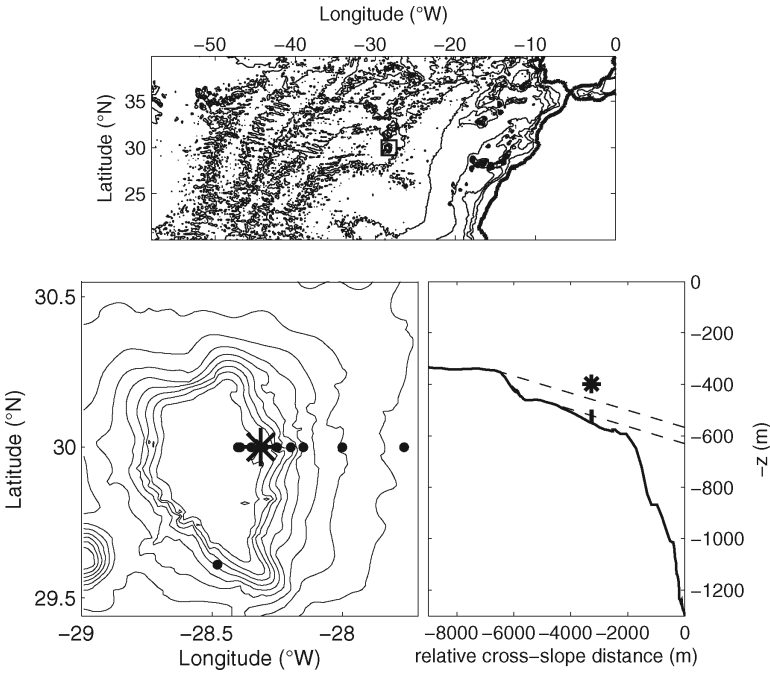


Figure 1. Location of mooring (*) and CTD/LADCP stations (•) near the top of Great Meteor Seamount (GMS). Bathymetry is computed from 1’-topography, an update from (Smith and Sandwell, 1997). In the overview panel, depth contour lines are every 1000m in the range [0, 5000] m. In the detail, every 500m for [500, 4500] m. Above the 3-D slope, projected on 2-D commensurate measured tilt, thermistor string extent (vertical bar), upper acoustic current meter (*) and M_2 -internal tidal wave rays (dashed) are indicated.

density (ρ) variations are dominated by temperature- (T) over salinity- (S) variations, by an absolute factor of 1.5-2 with S decreasing with depth like T (or potential temperature θ) (Fig. 2a-c). The linear relationship $\delta\rho = -0.101 \pm 0.002\delta\theta$ is reasonably tight (Fig. 2e) and the moored T-data are an adequate tracer for density variations. The local stratification, averaged over the range in Figure 2, amounts $N = 3.6 \pm 1.5 \times 10^{-3} \text{ s}^{-1}$ ($5.7 \pm 2.4 \times 10^{-4} \text{ Hz}$). Over smaller vertical scales in thin layers $O(1 \text{ m})$ N_{1m} varies over more than a decade (Fig. 2d). This stratification results in an average semidiurnal internal tide slope of 1.9° , so that the local bottom slope is significantly different from critical. However, numerical models demonstrate internal tide generation is nearby at slightly smaller depths (Fig. 1c; e.g., Gerkema and van Haren, 2007).

3. Computing turbulence parameters estimates using NIOZ-thermistors

We estimated the turbulence dissipation rate ε and vertical turbulent eddy diffusivity K_z by calculating “Thorpe scales” L_T using 0.5-m binned NIOZ thermistor-data over 50-m

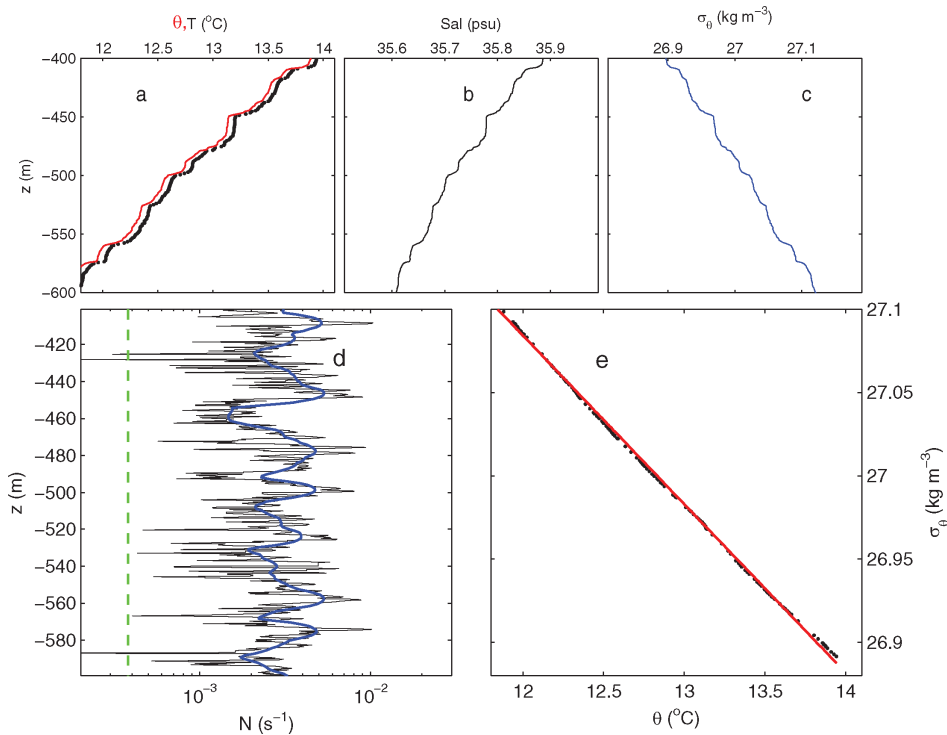


Figure 2. Sample CTD-profile near the GMS-mooring across the depth range expected to affect the moored instrumentation. (a) Temperature (black) and potential temperature (red). (b) Salinity. (c) Density anomaly referenced to the surface. (d) Buoyancy frequency using vertical separation $\Delta z = 1$ m ($N_{1\text{m}}$; black) and $\Delta z = 10$ m (blue) (excluding inversions), compared with hypothetical stratification due to (negative value of) adiabatic lapse rate (green). (e) Relative potential temperature-density relationship from CTD-observations (dots) of the profile in (d). The straight (red) line fit gives $\delta\rho = -0.101 \pm 0.002\delta\theta$ for the average of five such profiles. The timing of the profiles is arbitrary in the tidal period, but does not affect the relationship as the standard-error is a result of comparing all five profiles.

long profiles every 1 s. L_T is a vertical length scale of turbulent overturning in a stratified flow (Thorpe, 1977). It is obtained after reordering an observed potential density profile, which may contain inversions associated with turbulent overturns, into a stable monotonic profile without inversions. After comparing the raw and re-ordered profiles, the vertical displacement (d) necessary for generating the stable profile is assumed to be adiabatic as if the turbulent process is completely reversible. A certain threshold applies to disregard apparent displacements associated with instrumental precision. This is very low for NIOZ thermistor data, <0.5 mK the relative accuracy (van Haren *et al.*, 2009). Then, L_T is defined as the root mean square of the displacements within each overturn, and it is compared

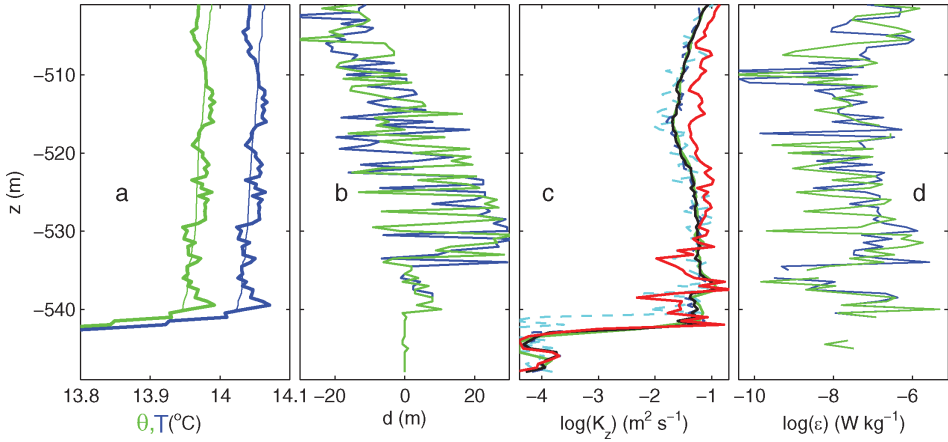


Figure 3. Overturning scale computation using NIOZ3 temperature data under weakly stratified conditions and for different averaging. (a) Temperature (blue) and potential temperature (green): raw (thick lines) and after reordering (thin) for day 146.5719. (b) Corresponding displacements. (c) Vertical profiles of (logarithm of) mean eddy diffusivity values over 860 s range of yeardays [146.565–146.575], for different averaging: directly averaged [K_z] (black), using 0.07-Hz (every 15th) data points (blue), using 0.01-Hz (every 100th) data points (light-blue), and computing a time-‘mean’ [K_z] after first averaging the heat flux and dividing it by mean potential temperature gradient (red). Averaging method is the same for the green curve as for the original 0.5 m-data, but it uses half the number of points in the vertical (1 m-data). (d) Corresponding dissipation rates.

with the turbulent Ozmidov scale $L_O = \varepsilon^{1/2} N^{-3/2} = 0.8L_T$, where the constant value is empirically determined (Dillon, 1982). N denotes the buoyancy frequency computed locally from the reordered profile. Rewriting we find,

$$\varepsilon = 0.64L_T^2 N^3, \quad (1)$$

and, using the relation $K_z = \Gamma \varepsilon N^{-2}$ (Osborn, 1980) with a constant mixing efficiency $\Gamma = 0.2$ for conversion of kinetic into potential energy,

$$K_z = 0.128L_T^2 N. \quad (2)$$

Initially, we hesitated computing (1) and (2) using the present data because we considered Thorpe’s original method was more suited for profile data at vertical resolutions better than 0.5 m, e.g., available from microstructure profiler or raw-CTD. The consequence will become clearer near the end of this section. Also, we had to correct for compressibility and slight pressure compensation in the NIOZ3-thermistor data that could spoil overturn estimates in very weakly stratified data. Figure 3 demonstrates that the present data are from such a vigorous overturning or strongly stratified area that the above constraints are

significantly smaller than the physical data and the 1-Hz time-series of vertical profiles provide a unique set of overturning estimates.

A test using data from a weakly stratified period shows that compressibility little affects L_T , but to some extent N , for which the square root of the adiabatic lapse rate coincides in absolute value with minimum N_{1m} (Fig. 2). A transfer of T to θ yields marginally (8%) larger K_z and ε for the example in Figure 3. Nevertheless, for the sake of completeness we will use θ henceforth.

Given the above tight $\delta\rho$ - δT relationship and the large signal-noise ratio, the two tests defined by Galbraith and Kelley (1996), a run-length and water mass property test, are easily satisfied for computing overturns from the present temperature data as a representative for density variations. Due to the occasionally large (> 10 m vertical) overturns, we are obliged to create a vertically complete data set, without sensor gaps. Therefore, the gaps by the three failing sensors are linearly interpolated, so that the vertical scale of 0.5 m is retained throughout the 50-m range. A comparison with 1-m binned data (skipping every other data point in the vertical) shows that, in this area, some resolution is lost in the vertical but otherwise similar results are obtained on turbulent overturning (Fig. 3). A later (Section 4) comparison of thermistor string estimated turbulence parameter values with a limited set of values estimated from CTD/LADCP data obtained in the vicinity of the mooring confirms the solidity of the former rather coarsely vertically sampled estimates.

As a consequence of the various scales of overturning, we compute (1) and (2) using individual displacement data for $L_T = d$ rather than their rms-value within an overturn, because it is too difficult to find the precise boundaries of each of the individual overturns. Small overturns appear in larger ones as is typical for turbulence (Fig. 3a,b). As a result, the higher K_z -values may be found at the edges of an overturn, which is thus not an artifact, but merely an effect of the lack of "overturn-averaging." Subsequently, after presenting the [0.5-m; 1-Hz] data they are averaged both in the vertical, over the entire range of 50 m, and over time, varying between a few hours to the entire period of a fortnight.

Several tests are made to validate the computation of turbulence parameters in the present dataset. First, a comparison is made between averaging K_z and computing an average K_z from averaging heat fluxes $K_z d\theta/dz$ divided by a mean temperature gradient. The latter is considered more correct, but in general the result is very similar (Fig. 3c); both averages will always be presented for comparison. Second, as the computation of overturns for all 1-Hz data in the entire two-week record is time-consuming, a test is performed by averaging subsampled data sets. Arbitrarily, short-period test-averages of 0.07 and 0.01 Hz subsampled data are compared to those of the original 1-Hz data. The short-period average profiles are noisier the less data are used, but the overall image is similar (Fig. 3c) so that a two-week data set can be investigated with confidence albeit lacking the 1-Hz details.

We compare the above turbulence estimates under stratified conditions with several parameterizations. Dissipation rate and vertical heat flux are directly proportional to each other, $K_z d\theta/dz \propto \varepsilon$. As a threshold for transition to isotropy in stratified waters, a value of $\varepsilon = 200\nu N^2$, $\nu = 10^{-6} \text{ m}^2 \text{ s}^{-1}$ kinematic viscosity, is used (Gargett *et al.*, 1984). The energetic turbulence regime is considered for $\varepsilon/(\nu N^2) > 200$.

Combining with (1) this threshold condition leads to,

$$L_T > \left(\frac{200\nu}{0.64N} \right)^{1/2} = 17.7\delta, \quad (3)$$

where $\delta = (\nu/N)^{1/2}$ a laminar Ozmidov scale, proportional to the Kolmogorov scale and used by Gargett (1988) as the stratification-squashed vertical length-scale under low (non-oceanic) Reynolds numbers. For the present mean N , threshold value $L_T > 0.3$ m, which is smaller than the separation between the thermistors, so that we expect to estimate exclusively the energetic turbulence regime.

Gregg (1989) reviewed several scalings for $\varepsilon \sim N^{+1}, N^{+3/2}, N^{+2}$, the latter being perhaps the most appropriate one in the case of constant gradient Richardson number and shear amplitude $|S| \sim N$. For these scalings, N was averaged over a significant amount of time. Recast in terms of eddy diffusivity, using the Osborn model, would give $K_z \sim N^{-1}, N^{-1/2}, N^0$ for above dissipation rate parameterizations. Arguably, one could investigate $\varepsilon \sim N^0, K_z \sim N^{-2}$, which yields a classic stratification squashing turbulence, together with several other parameterizations ($K_z \sim N^{+1}, N^{+2}$; as partially demonstrated for different shear wave-number regimes by Gargett *et al.*, 1981). We will explore such parameterizations and compute best linear fits between average K_z and powers of N in Section 4 for different phases in a tidal (turbulence) period.

4. Observations

Eqs. (1) and (2) are applied to the GMS NIOZ3 thermistor data in several stages of short periods of time together describing a particular tidal period. This tidal period contains the largest frontal bore in the entire 18-day record, but is otherwise arbitrarily chosen. From the entire record it is seen that this period is just before spring-tide (Fig. 4a), when the barotropic tidal current amplitude is about 0.15 m s^{-1} (not shown; observed locally using current meters and verified using TPXO7.2). The tidal isotherm displacements well exceed the 50 m thermistor string range (Fig. 4b).

For investigation, the tidal period will be split in three parts, each describing different turbulent characters of internal tidal motions above sloping topography. First, the change is described from warming, down-slope motion to the cooling, upslope tidal phase associated with the passage of a frontal bore. This period generally describes largest mixing, if the front is sharpened enough. Second, the entire cooling phase is investigated. Third, the entire subsequent down-slope warming phase is presented. Following the detailed description of the tidal period, the whole two-week record is discussed, including its spectral image. Turbulence parameters are also estimated using ship-borne CTD/LADCP data, for comparison.

a. A frontal change of tidal phase

The sudden change from warming to cooling tidal phase associated with an upslope moving frontal bore renders an image of massive turbulent eddy diffusivities and associated

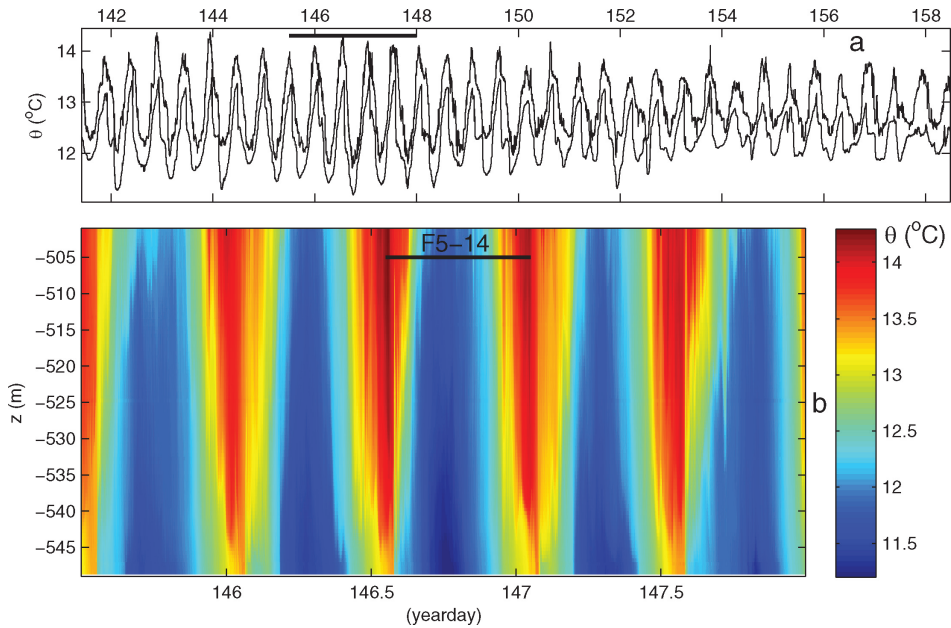


Figure 4. Overview of potential temperature data. (a) Total time series at upper and lower thermistors. The bar indicates time span of the lower panel. (b) Depth-time series of 2.5 days detail, with the bar indicating the tidal period treated in detail in Figures 5–14.

turbulence dissipation rates (Figs. 5–7). Comparing the raw data (Fig. 5a) with the reordered profile (Fig. 5b) already enlightens part of the raw turbulence associated with the large backward breaking wave: the turbulence-image has the lighting of a 3D-image like 17th-century Dutch paintings, whilst the stably reordered image has an essential 2D appearance. The reordering clearly straightens the large front that was originally curved.

The reordered stable stratification (Fig. 5c) shows very thin (down to lowest resolution $\Delta z = 0.5$ m) layering, approaching the bottom to within a meter just prior to the frontal passage. Subsequently, this layered stratification is found throughout the range of observations without indicating a particular homogeneous ‘bottom boundary layer.’ Associated displacements (Fig. 5d) beautifully delineate the turbulent patches or overturns, and overturns within overturns down to about the scale of vertical resolution. The largest displacement values are found near the edges of a patch, as expected (Fig. 3). Typical patches have sizes of 10 m in the vertical and 300 s in time, but smaller and also larger ones occur, even exceeding out-of-range of the thermistors (e.g., day 146.57 in Fig. 5d). This exceeding leads to an unknown low-bias.

Such large displacements are observed at, but especially also in the half hour before, the arrival of the big front. This is thus where large eddy diffusivity (Fig. 6a,b) is estimated, locally up to $K_z = 10^{-1} - 10^0 \text{ m}^2 \text{ s}^{-1}$. There is a distinct difference between large values coming from above, as just before arrival of the big front reaching down to about 10 m

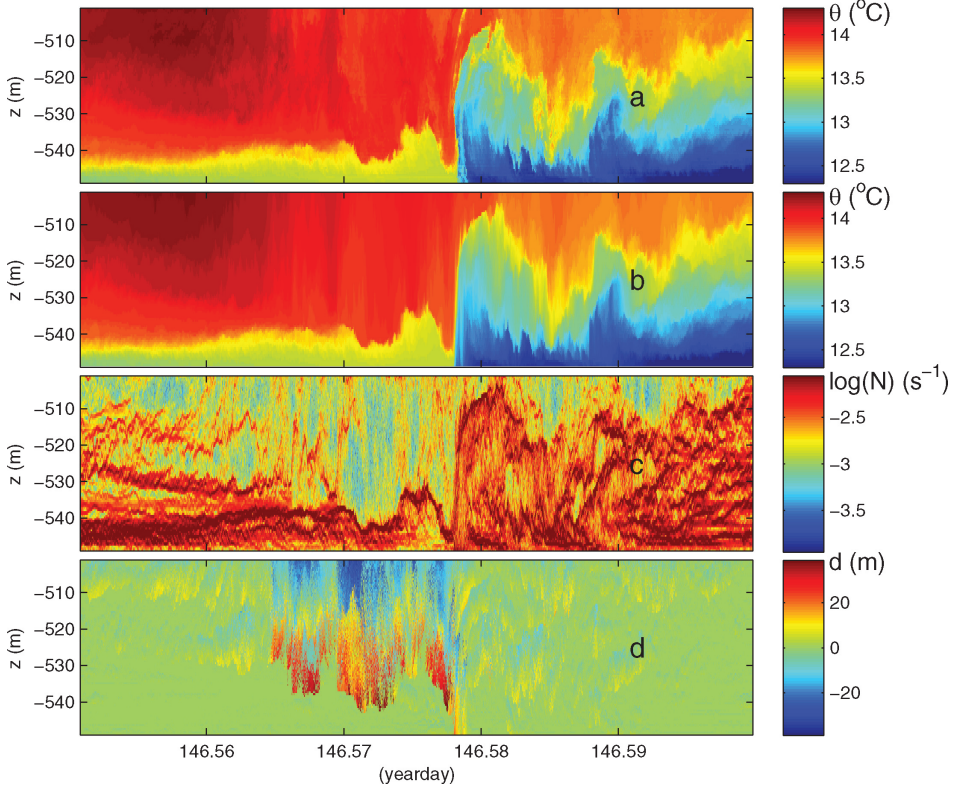


Figure 5. Depth-time series of potential temperature and computed variables during 75 minutes prior to and into an upslope tidal phase: a frontal passage and associated peaks in turbulent mixing. The three missing thermistors have been linearly interpolated between their neighbors. (a) Potential temperature data, after pressure-corrected calibration of raw temperature data. (b) Re-ordered potential temperature profiles every 1-Hz time-step. Reordering is performed as if temperature variations inversely represent density variations, using the tight relationship of Figure 2b. (c) Stable stratification computed from (b), using the relationship to Figure 2e. (d) Thorpe displacements following comparison of (a) and (b).

from the bottom, and those reaching up from the bottom at and immediately after the frontal passage. The pre-frontal vertical motions reach down to -0.15 m s^{-1} , as observed in simultaneous current measurements (not shown).

Large K_z -values are generally estimated within layers of weaker stable stratification, with exceptions of high values in thin strongly stratified layers such as those forcing the big front. Physically, it is better to consider the heat flux (Fig. 6c), which renders a more even distribution than K_z for the dominant periods. The front stands-out more clearly in both the heat-flux and eddy-dissipation rate (Fig. 6d) images.

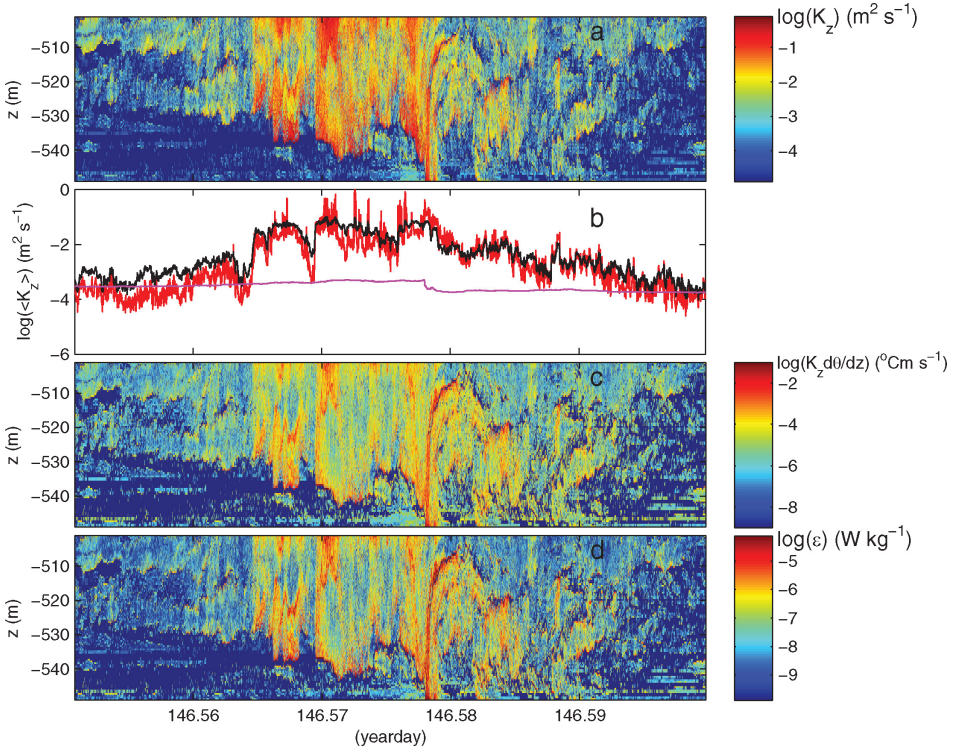


Figure 6. Computed variables on mixing results for data in Figure 5. (a) Eddy diffusivity computed using (2) for all of the individual displacements in Figure 5d. (b) Time series of vertically averaged K_z (black) and after first averaging heat flux (red), with for comparison mean N^{-2} (purple). (c) Heat flux after multiplication data in (a) with stable re-ordered potential temperature gradient. (d) Turbulence dissipation rate, estimated using (1). In (a),(c),(d) dark-blue also indicates below threshold.

Averaging over depth (Fig. 6b) and time (Fig. 7) equally shows the dramatic impact of the upslope frontal passage and its pre-surge vigorous turbulence period. Averaging over depth shows the same large variability in time as was visible in the depth-time series. In this sample, the variability has the same periodicity of about 500 s as the local thin-layer buoyancy period. This suggests that the turbulent patches are powered in part by the extreme shortest freely propagating internal waves. Vice versa, the former may force the latter, as a direct consequence of shoaling bore forcing its way up the slope. Large-scale N varies considerably less with time (Fig. 6b; purple graph).

Averaging over time provides very similar vertical profiles for different ways of averaging, with the vertically most variable one using the most correct ‘flux-averaging-method’ (Fig. 7). Nonetheless, there is not a really significant difference between this (red) profile and the black one resulting from directly averaging eddy diffusivity. When compared to profiles of

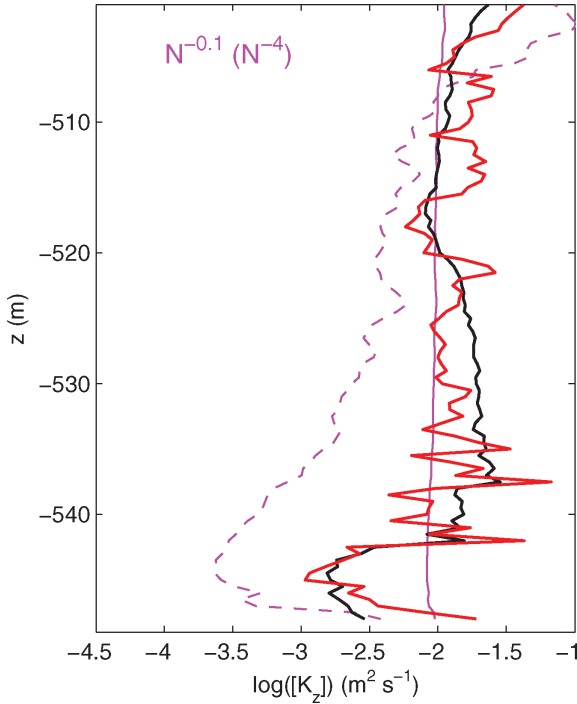


Figure 7. Time-mean profiles for data in Figure 6a (black) and after first averaging of heat flux (red). For comparison, two profiles of different powers of mean stratification (in s^{-1}) are given with arbitrary x-offsets: computed best linear fit to $\log(N)$ - $\log(K_z)$ between $[-544, -494]$ m (solid purple) and an eye-fit (dashed purple, value between brackets).

various powers of buoyancy frequency/period, the best fit in the z -range $[-544, -499]$ m is obtained for $N^{-0.1}$. Portions of the profile fit better various powers of N with the mean eddy diffusivity resembling N^{-2} ($[\epsilon] \sim N^0$) for $z > -518$ m. Between $-538 < z < -518$ m $[K_z] \sim N^{+1}$, reversing power sign again up to N^{-4} in the near-bottom layer.

b. An upslope phase

Similar turbulence variability although at different, smaller and weaker scales compared to those of the frontal bore, is found during the upslope, cooling tidal phase following the bore (Figs. 8–10; note some different (color) scales compared to Figs. 5–7). During such a phase, turbulence initially mainly occurs in the stratified interior in patches of typically 1–10 m thickness. They are part of the trailing waves behind the frontal bore and do not reach the bottom. These waves move out of range of the thermistors within half an hour and it is obvious that the combined locally enhanced stratification and decreased overturning cause rapidly decreasing turbulence parameters to background levels, e.g., $<10^{-4} m^2 s^{-1}$ for K_z . However, some time during the upslope phase away from the frontal bore and closer

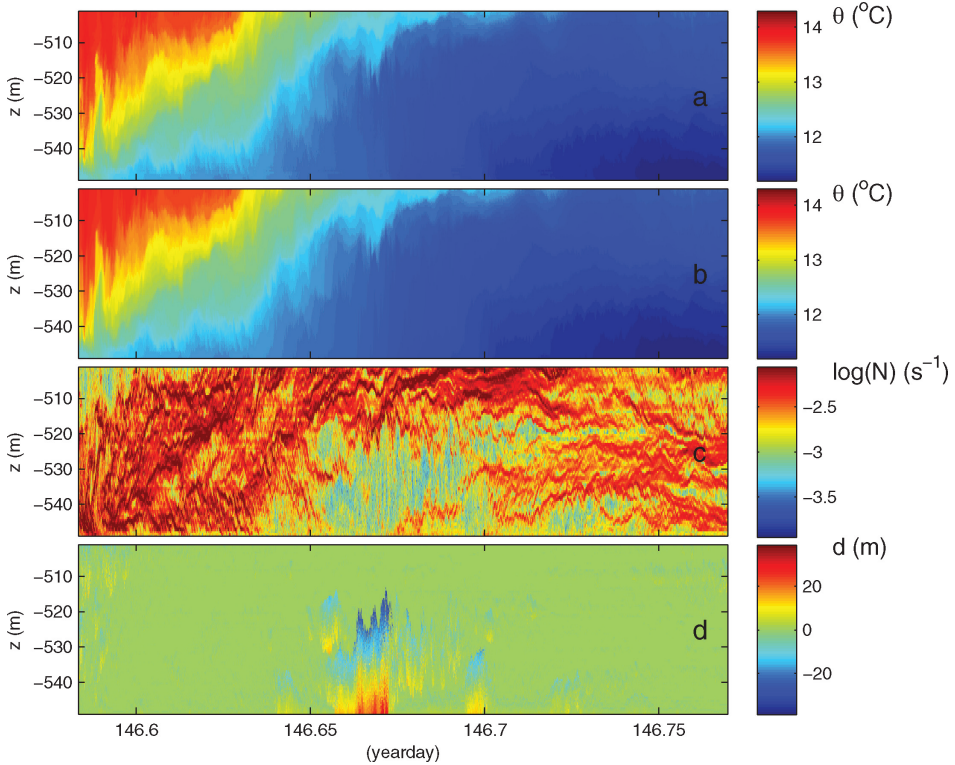


Figure 8. As Figure 5, but for 4.5 hours of total upslope, cooling tidal phase including and following the front of Figure 5. Note different color-scales in temperature panels compared to Figure 5.

to the moment of weakest near-bottom stratification a renewed turbulence patch follows. It extends from the bottom upward, albeit less intense than the first front. In the present example it is associated with the weakly stratified portion of a relatively large ‘bottom boundary layer’, but part is also due to a local weak secondary front. Like the frontal bore, its relative contribution to overall mixing varies with each tidal cycle. During this moment in the tidal phase, small turbulence patches are rarely observed in the interior. Nonetheless, the secondary near-bottom and these interior patches can reach values of $K_z = 10^{-3} - 10^{-1} \text{ m}^2 \text{ s}^{-1}$, $\varepsilon = 10^{-6} - 10^{-5} \text{ W kg}^{-1}$, even though some are short-lived $O(10^2 - 10^3) \text{ s}$.

Averaging over time again provides similar vertical profiles for different ways of averaging, but now at time-mean values $10^{-4} < [K_z] < 10^{-2} \text{ m}^2 \text{ s}^{-1}$ (Fig. 10). For this upslope tidal phase it is seen that $[K_z]$ linearly fits N^{-4} for $[-544, -499] \text{ m}$, whereas N^{-8} better corresponds with the dynamical spread over the vertical range. However, the precise height where their maxima (near 520 m) and subminima (near 540 m) are found differs by about 5 m.

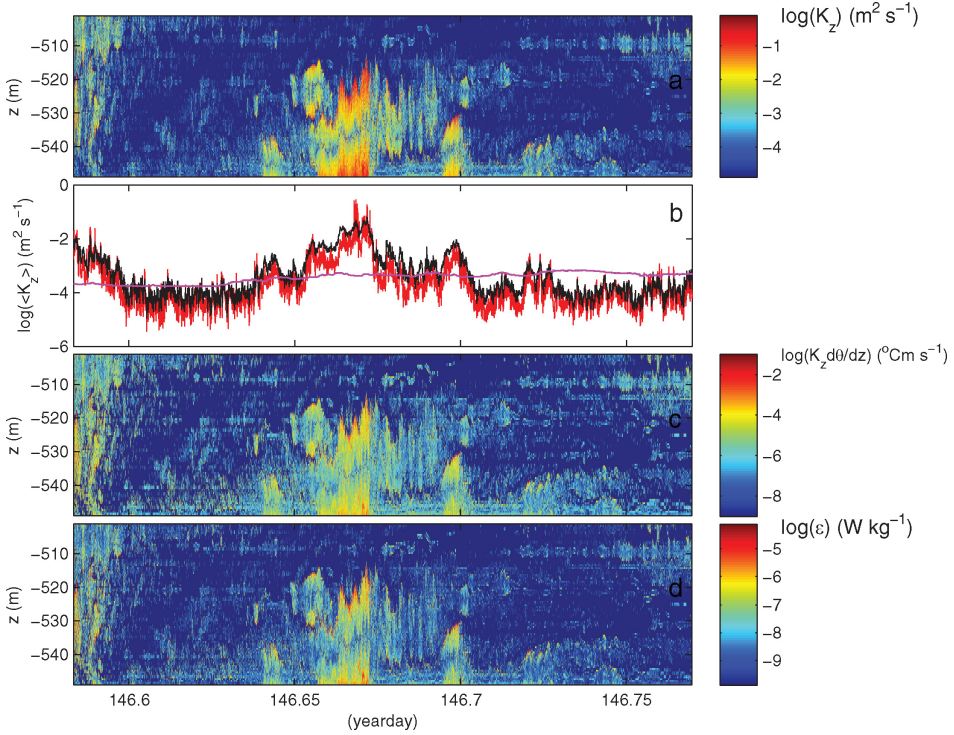


Figure 9. As Figure 6, but for data of Figure 8.

c. A downslope phase

Quite different and less intense turbulence is found during a downslope, warming tidal phase (Figs. 11–13). During such a phase, turbulence mainly occurs in the stratified interior in patches varying between about 5 and 15 m in thickness, not reaching the bottom although occasionally approaching it to within a meter. Turbulence is organized in billows, either associated with apparent locally mode-2 isopycnal split-ups or with overturning Kelvin-Helmholtz (K-H) instabilities (not visible in large-scale Figure 11; for detail cf. van Haren and Gostiaux, 2010). Although being weaker in general, turbulence can reach values of $K_z = 10^{-3} - 10^{-2} \text{ m}^2 \text{ s}^{-1}$, $\epsilon = 10^{-7} - 10^{-6} \text{ W kg}^{-1}$. In periods with little overturning, e.g., regularly between days 146.95 and 147, values drop to calm, stably stratified “open ocean” values $K_z < 10^{-4} \text{ m}^2 \text{ s}^{-1}$, $\epsilon < 10^{-8} \text{ W kg}^{-1}$. Such periods are interrupted by short-lived peaked increases in turbulence parameter values, following turbulent overturning somewhere in the interior. They can be quite intense during the weakly stratified period immediately following the transition to downslope phase (between days 146.8–146.92 here), but especially also when supported by the larger stratified thin layers later in this tidal phase. Some of these overturns develop as 50-s K-H billows (van Haren and Gostiaux, 2010), which

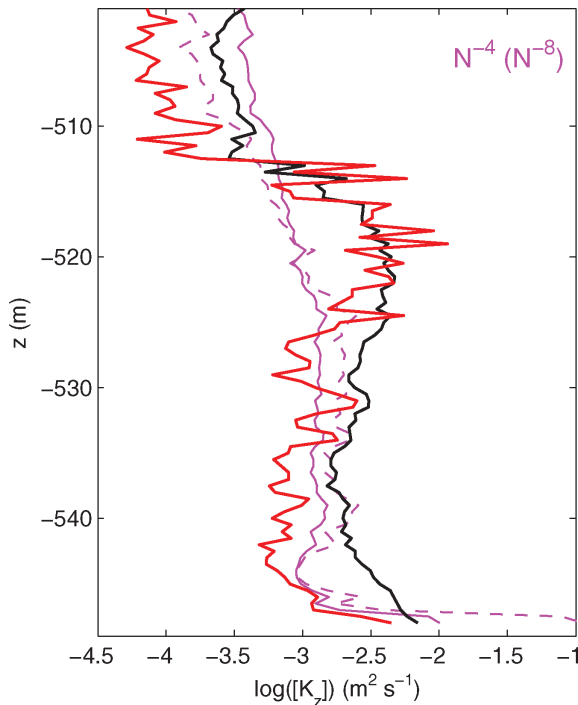


Figure 10. As Figure 7, but for data of Figure 8.

stand-out in flux- and turbulent dissipation rate depth-time series, in an otherwise quiescent environment.

The 50-s variability, far shorter than any possible [thin-layer] buoyancy periods, is retrieved in the depth-averaged turbulence parameters like K_z . The billows are carried by larger internal wave motions. Typical advective current speeds are 0.1 m s^{-1} , but as we have no information on direction of propagation of short-scale internal waves with respect to larger-scale tides, it is hard to establish billow-sizes in a moving frame of reference. This 50-s variability is not only dominant during the passage of a K-H billow train, but basically during the entire record whilst sometimes being less important than larger scale variations up to 500 s, the thin-layer buoyancy period (e.g., day 147.0).

Averaging over time of this tidal phase gives mean values $10^{-4} < [K_z] < 2 \times 10^{-3} \text{ m}^2 \text{ s}^{-1}$ (Fig. 13). For such downslope tidal phase period, it is seen that $[K_z]$ fits best $N^{-1.3}$ for the range $[-544, -499] \text{ m}$. It resembles the N^{-2} profile for $z < -536 \text{ m}$. Between $-542 < z < -536 \text{ m}$ it resembles more or less N^{+2} , whilst N^{+8} or so very close to the bottom.

d. Two-week period

The above tidal period observations are summarized in one graph (Fig. 14). Over the entire two-week record, the depth-averaged turbulence is seen to vary with tidal period

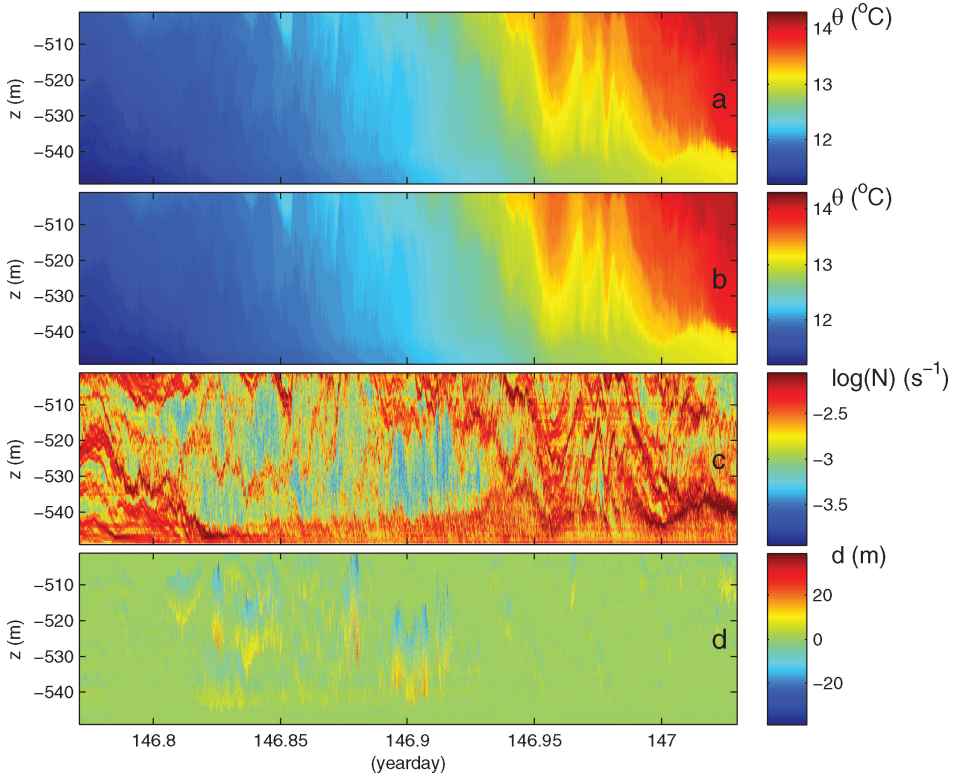


Figure 11. Nearly 6.2 hours of total downslope tidal phase following Figure 8.

including a weakly visible spring-neap period, but it is most dominantly-peaked over periods shorter than tidal due to (non-linear) frontal passages (Fig. 15). The semidiurnal and some higher frequency variations are more visible in the mean stratification time series ($\langle N^{-2} \rangle$, purple graph in Fig. 15a), but $\langle N^{-2} \rangle$'s one decade variation in value over the whole time span is much less than the four decades found in $\langle K_z \rangle$ (or $\langle \varepsilon \rangle$), despite the occasionally in-phase variability. Only when data are 2-hourly smoothed the resulting 2-decade dynamic range of turbulence parameters matches the range of $\langle N^{-4} \rangle$ (Fig. 15b). As noted, tidal periodicity variations of $\langle \varepsilon \rangle$ and $\langle N^{-4} \rangle$ differ from regularly out-of-phase (days 146–150) to mostly in-phase (155–158). The long-term, subinertial variations of a 3–4 days (intermittency) and (weak) spring-neap variability, compare $\langle \varepsilon \rangle$ best with $\langle N^{+4} \rangle$. Tidal motions thus generate turbulence, but not only in a direct manner but especially also intermittently via nonlinear interactions. Turbulence remains very energetic and exceeds the “Reynolds number” threshold of depth-mean $\langle \varepsilon \rangle / (\nu \langle N^2 \rangle) > 200$ nearly always, with factors times the threshold reaching up to 10^4 (Fig. 15b).

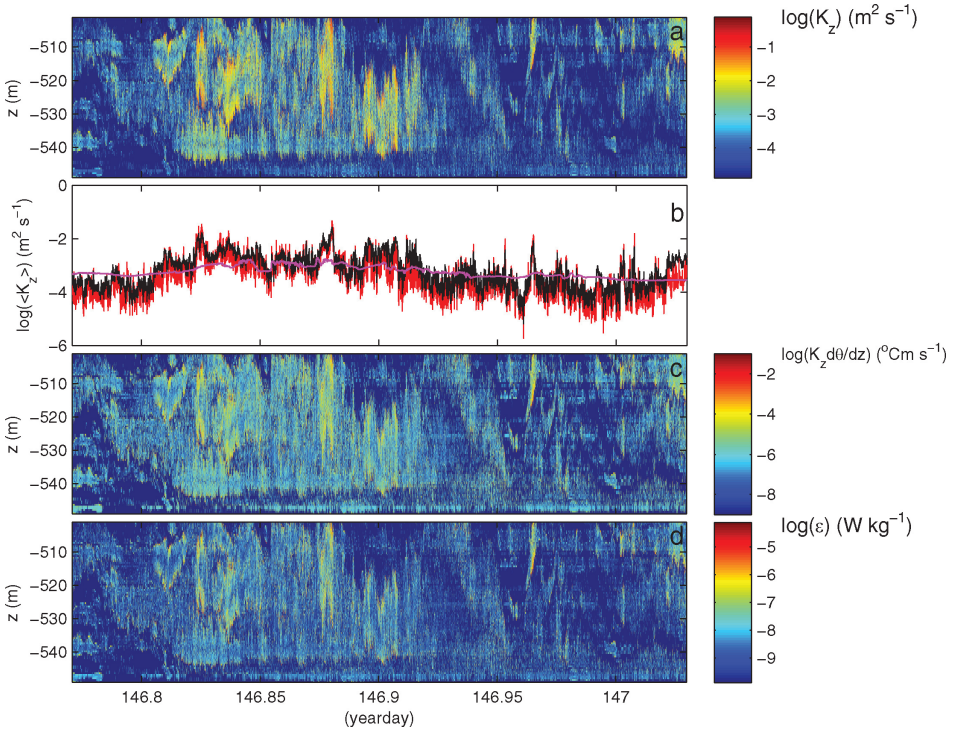


Figure 12. As Figure 9, but for data of Figure 11.

Averaged over time, nearly uniform profiles of turbulence parameters are observed, with mean $[K_z] = 1.5\text{--}4 \times 10^{-3} \text{ m}^2 \text{ s}^{-1}$ (Fig. 16), $[\epsilon] = 1\text{--}2 \times 10^{-7} \text{ W kg}^{-1}$. As for the shorter periods, the comparison with mean buoyancy frequency profiles shows ambiguous model results in powers of N at different depths, although in this case the (small) dynamic range is quite small. The best fit is found for $N^{+0.6}$ (solid) over the z -range $[-544, -499]$ m. Above $z > -535$ m N^{+2} (dashed) fits better, whereas for $z < -538$ m only negative powers of N would fit.

A comparison between turbulence parameters and dynamic variable bottom-pressure (p) yields no conclusive results: except for tides none of the signals are significantly coherent at the 95% significance level over the two-week period. Nevertheless, a comparison between spectral slopes yields useful information on internal wave-turbulence aspects in variables like p and T , designating various frequency bands, for an area above sloping topography that is expected to be more turbulent than the ocean interior. The internal wave-turbulence character is to be compared with long surface “infra-gravity” waves (IGW), which partially occupy the same frequency band. The overall spectrum of depth-mean K_z (Fig. 17; red curve) resembles the slope of the bottom pressure spectrum (blue) in the internal wave (continuum; IWC) band, while the logarithm of turbulent heat flux (green) adopts a $-5/3$

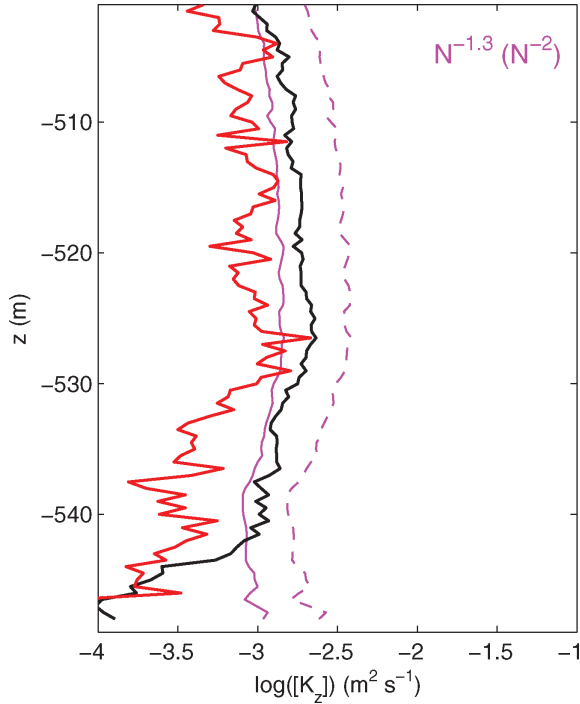


Figure 13. As Figure 10, but for data of Figure 11.

slope. Apart from a transition band between $10^{-3} < \sigma < 10^{-2}$ Hz, the logarithm(heat flux) maintains a $-5/3$, say Kolmogorov-turbulence, slope with frequency for $\sigma > 10^{-2}$ Hz, well to within statistical error bounds. Apparently, the operation of multiplying K_z with $d\theta/dz$ leads to a turbulence spectrum, with a transition in the (small-scale) buoyancy frequency range (\sim IGW). This remarkable observation suggests a direct transfer between internal waves and turbulence.

The eddy diffusivity itself matches the slope of the bottom pressure spectrum not only in the IWC but also deviating from the IWC-slope into the IGW-band. This confirms the time series observation of K_z -periodicities of 30–500 s, significantly smaller than the small-scale maximum buoyancy period $2\pi/N_{1,\max}$. For $\sigma > N_{1,\max}$, pressure and eddy diffusivity spectra differ slightly, which is where logarithm(heat flux) re-adopts the $-5/3$ slope. At $N_{1,\max}$, the bottom temperature spectrum suddenly changes slope from $-7/3$ to $-5/3$. A similar change in slope has been observed for bottom pressure in a turbulent regime delineating the transition from low to high wavenumbers (Gotoh and Fukayama, 2001). In the present data, there is no match between turbulence parameters and the bottom-pressure due to surface wind waves (SW), which are very small at 549 m water depth.

The smooth transition between IWC and IGW for both bottom-pressure and eddy diffusivity questions the general idea that the deep-ocean bottom-pressure IGW-band is mainly

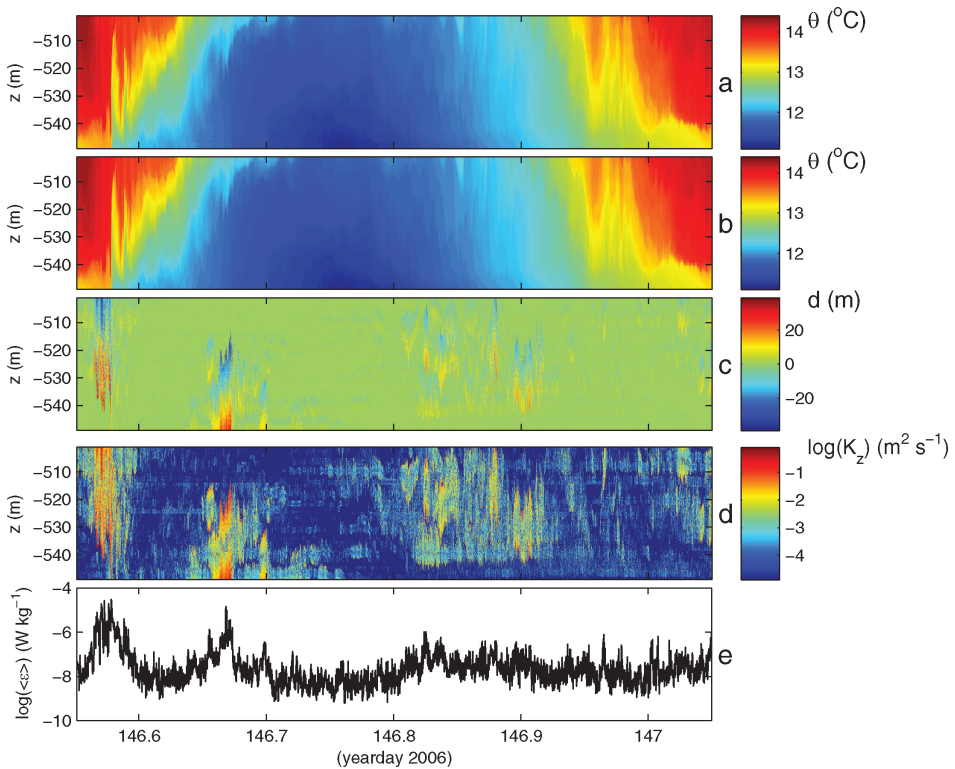


Figure 14. Overview of one tidal period of Figures 5–13, using 0.1 Hz sub-sampled data.

due to large-scale nonlinear surface waves crossing entire ocean basins (e.g., Webb *et al.*, 1991). Such low-frequency surface waves cannot induce the observed turbulence and would not appear in the K_z -spectra. It is thus concluded that, in the present data above sloping topography, turbulence dominates this band, and that the turbulence is generated by and extends smoothly into the internal wave continuum band. This internal wave band is fed by near-inertial motions, especially tides, their intermittently occurring non-linear parts, high-frequency waves near the buoyancy frequency and modulation of the stratification they are supported by.

e. Independent shipborne data

The above high-resolution time series observations are confirmed to within a factor of three by CTD/LADCP data (Fig. 18). A short transect shows typical values of $K_z = 0.3\text{--}1 \times 10^{-3} \text{ m}^2 \text{ s}^{-1}$, $\epsilon = 0.5\text{--}1 \times 10^{-7} \text{ W kg}^{-1}$ at and above the depth of the bottom lander mooring. Values from limited LADCP-data are obtained from profiles averaged in 100 m vertical bins, basically using the method and stratification- and shear-scaling as in

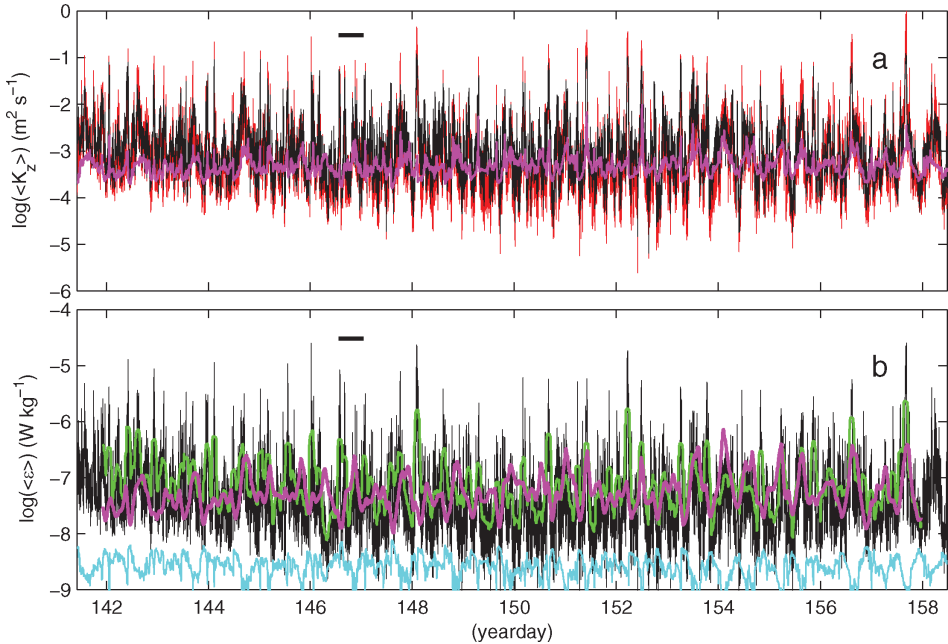


Figure 15. Total time series of vertically averaged variables using 0.01-Hz data (data points every 100 s). (a) Mean $\langle K_z \rangle$ (black) and after first averaging heat flux (red), with for comparison mean $\langle N^{-2} \rangle$ (purple; arbitrary logarithmic scale). (b) Mean turbulent dissipation rate (black) its 2-hourly smoothed version (green) and 2-hourly smoothed $\langle N^{-4} \rangle$ (purple; arbitrary scale), with mean ‘Reynolds number threshold’ $200v\langle N^2 \rangle$ (light-blue) for comparison. The tidal period of Figures 5–14 is indicated by the black bar.

Gregg (1989). This implies the use of parameterization involving a full cascade of energy from source to dissipation. More detailed near-bottom values turn out to be larger than above values, by a factor of about 2. Otherwise, the shipborne CTD and LADCP turbulence parameter estimates show a good comparison, but it is noted that smoothing is rather heavily and the transect is just a snap-shot.

5. Discussion

In several ways GMS compares well with tidal energy budgets observed above the Hawaiian Ridge, a dominant internal tide generator in the Pacific. Per seamount, tidal conversion from barotropic to baroclinic energy is very similar (0.3 GW; Klymak *et al.*, 2006; Gerkema and van Haren, 2007; van Haren *et al.*, 2010). Mean dissipation rates vary between 10^{-8} – 10^{-7} W kg $^{-1}$, which are found at various critical and noncritical internal tide slopes and which are much larger than found in the interior (Levine and Boyd, 2006; Aujan *et al.*, 2006). The latter authors show that the less clear tidal and spring-neap cycles in turbulence

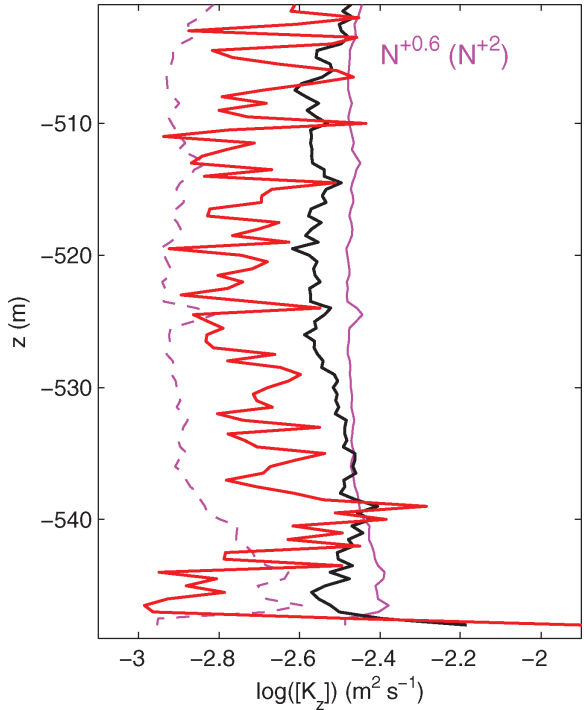


Figure 16. As Figure 7, but for total data set (0.01 Hz data), averaged over a fortnight. Note the different horizontal scale.

parameter time series is due to peaks at the change of warming to cooling phase (the frontal bore here) and during the upslope phase (the secondary front here). The present data reveal more detailed bursts of 900–3000 s duration, with 2–4 large peaks in a tidal period, not just one as found in recent LES modeling (Gayen and Sarkar, 2011) that otherwise resembles the present observations quite well.

If we use Armi’s (1979) and Garrett’s (1990) suggestion that 3–30% of the ocean is occupied by bottom boundary layers above sloping topography, we find an overall mean ocean-basin-interior $K_z \approx 3 \times 10^{-4} \text{ m}^2 \text{ s}^{-1}$, when we take a tenth of the mean K_z we estimated using the present high-resolution data and which was reported for a deeper Hawaiian Ridge slope by Aucan *et al.* (2006). Such basin-wide eddy diffusivity value would be sufficient to maintain the meridional overturning circulation, for which a canonical value of $10^{-4} \text{ m}^2 \text{ s}^{-1}$ is required (Munk and Wunsch, 1998). This supports earlier conjectures (e.g., Munk, 1966; Armi, 1978; Garrett, 1990) for the importance of sloping boundary mixing; but what are the caveats?

A potential caveat may be the universality of the present results for all slopes. A line of thoughts is that a dominant source of mixing is induced via tides, which are energetic motions and of which internal, baroclinic motions are most energetic when their slope

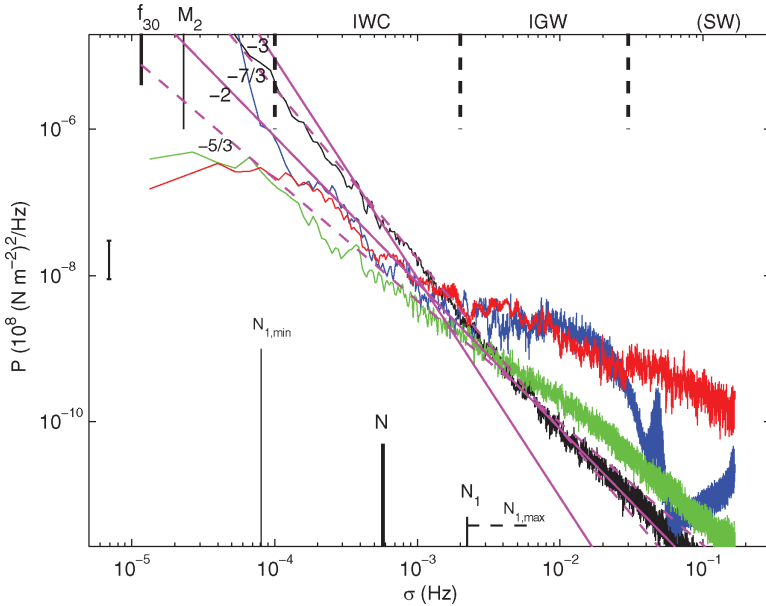


Figure 17. Two-weeks mean spectra for near-bottom pressure (blue), temperature (in $^{\circ}\text{C}^2/\text{Hz}$; black) and 50-m vertically averaged eddy diffusivity (in $(\text{m}^2 \text{s}^{-1})^2/\text{Hz}$; red) and logarithm of flux (in $(^{\circ}\text{C m s}^{-1})^2/\text{Hz}$; green). Except for pressure, all records are arbitrarily off-set vertically. Several wave-turbulence bands are indicated (see text), together with mean buoyancy frequency N and minimum and maximum small-scale ($\Delta z = 1 \text{ m}$) values. The straight purple lines indicate several slopes for guidance.

critically matches the bottom slope. However, here the bottom slope is not critical and noncritical vigorous bore-like motions have been observed elsewhere at shallower depths (e.g., Klymak and Moum, 2003), at similar depths (e.g., Hosegood *et al.*, 2004) and at much greater depths (Bonnin *et al.*, 2006). None of these depths was particularly critical in slope for tides. So, it is hypothesized that most sloping boundaries are important for deep-ocean mixing. Also, other mechanisms like lee wave formation may be important at super-critical slopes (Klymak *et al.*, 2010).

A second caveat may be the driving force. Existing models (Thorpe, 1987; Garrett, 1990) used boundary layers set-up for “constant” flows that are slowly varying compared to the inertial period. The present data show that variability of boundary layer height is much faster than that, not only on a tidal scale but even faster. As a result, the set-up of a well-defined boundary layer is not observed. But, this may not be so important, as it also means that the near-bottom stratification varies at the same fast pace as the boundary layer.

A third caveat may be the efficiency of mixing, which was concerned by Garrett (1990; 1991) who questioned a dramatic drop of efficiency once a boundary layer was well established. As noted above, the present data clearly show that a well-established boundary

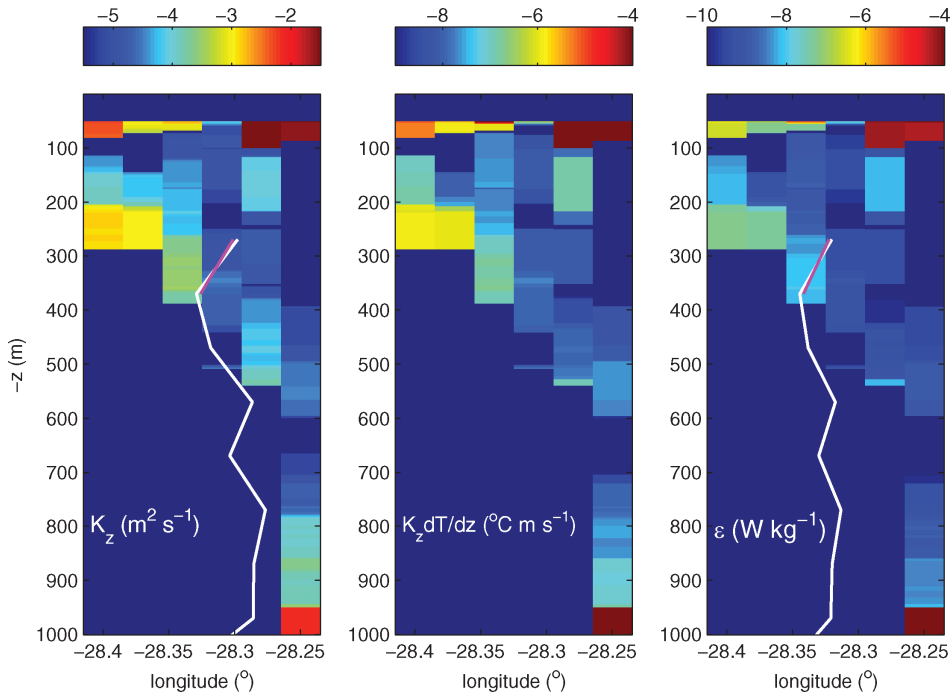


Figure 18. Short cross-slope transect passed the mooring site estimating turbulence parameters using shipborne CTD (colored values; computed from overturning scales) / LADCP (plotted profiles from shear&stratification data, with the same scale as the color bars on top). The purple curve is from 550 m, the white one from 2000 m water depth.

is never reached and stratification in varying intensity reaches all the way to the bottom, regularly or most of the time, so that efficient mixing is ensured. This may affect the transport of mixed waters away from the sloping topography and into the interior.

As for the transportation of mixed water into the interior, which constitutes a fourth potential caveat, the observed small-scale stratification and [backward] breaking bore-like waves do sweep material and fluid away from the boundary. This confirms numerical modeling by Slinn and Riley (1996), who addressed the importance of the action of internal waves in communication of mixed fluid into the interior. They estimated a mixing efficiency of as large as 35%. Such efficient mixing is evidenced here, as a considerable amount occurs in the stratified layers near, but away from the bottom, thereby facilitating mixed fluid transport along isopycnals into the interior. The local breaking and restratification occur at short, small-scale buoyancy periodic time scales, so that efficient mixing is guaranteed, also very close (<1 m) to the bottom.

It is thus the lower frequency, in this case tidal, motions, but especially the highly nonlinear deformations of their linear origins that drive the bottom boundary layer. This is different from a tidal frictional boundary layer above a flat bottom, where a direct transition from

source (tide) to turbulence occurs. Above slopes, the largest mixing occurring just prior to the change from down- to upslope phase may sharpen the front and thus effectively controls the intensity and release of the bore. In fact, it is hard to define a bottom boundary layer in a classic sense, as exemplified by Weatherly and Martin (1978). In the examples shown here, K_z -profiles only match a particular power of N parameterization in very limited depth and time portions. There are periods when $K_z \sim N^{-2}$ ($\varepsilon \sim N^0$; e.g., near-bottom of frontal bore) is found to be correct, but periods are also found when $K_z \sim N^0$ ($\varepsilon \sim N^{+2}$; the front most of the range except near the bottom) or $K_z \sim N^{+2}$ ($\varepsilon \sim N^{+4}$; 3–4 day periodicity) is more appropriate. This perhaps delineates a turbulent bottom boundary layer from a restratifying, buoyancy restoration dominated layer above.

The variations in N -scaling demonstrate that sloping bottom areas are not easily parameterized. Klymak *et al.* (2010) use a knife-edge model involving stratification and topographic slope. Perhaps shear should be involved besides stratification, although it has been taken into account by Gregg (1989). Future parameterizations should take the nonlinearity of internal wave motions into account, which seem to constitute the intermediate between the source (tides/inertial motions) and the sink (turbulence). If we scale-up with reference to the present observations, we see 30–50 s overturning billows governed by 900–3600 s internal waves near the (local, small-scale) buoyancy frequency that are associated with the tidal phase. The tide also couples with the large highly nonlinear bore-like overturns occurring once or twice in a tidal period. Their generation is strongly dependent on straining, or modification of stratification at all scales. Their arrival is (thus) intermittent, or a modulation of a few days.

Acknowledgments. We thank the crew of the R.V. *Pelagia* for deployment and recovery of our moorings and Theo Hillebrand and NIOZ-MTM for preparation of instrumentation. We greatly thank Martin Laan, Dirk-Jurjen Buijsman and Edwin Keijzer for construction of NIOZ-thermistors. Construction and deployment of ‘NIOZ3’ were financed in part by investment grants (‘Oceanographic equipment’ and ‘LOCO,’ respectively) from Netherlands Organisation for the Advancement of Scientific Research, NWO and by BSIK.

REFERENCES

- Armi, L. 1978. Some evidence for boundary mixing in the deep ocean. *J. Geophys. Res.*, *83*, 1971–1979.
- 1979. Effects of variations in eddy diffusivity on property distributions in the oceans. *J. Mar. Res.*, *37*, 515–530.
- Aucan, J. and M. A. Merrifield. 2008. Boundary mixing associated with tidal and near-inertial internal waves. *J. Phys. Oceanogr.*, *38*, 1238–1252.
- Aucan, J., M. A. Merrifield, D. S. Luther and P. Flament. 2006. Tidal mixing events on the deep flanks of Kaena Ridge, Hawaii. *J. Phys. Oceanogr.*, *36*, 1202–1219.
- Bonnin, J., H. van Haren, P. Hosegood and G.-J. A. Brummer. 2006. Burst resuspension of seabed material at the foot of the continental slope in the Rockall Channel. *Mar. Geol.*, *226*, 167–184.
- Dillon, T. M. 1982. Vertical overturns: a comparison of Thorpe and Ozmidov length scales. *J. Geophys. Res.*, *87*, 9601–9613.

- Galbraith, P. S. and D. E. Kelley. 1996. Identifying overturns in CTD profiles. *J. Atmos. Ocean. Tech.*, *13*, 688–702.
- Gargett, A. E. 1988. The scaling of turbulence in the presence of stable stratification. *J. Geophys. Res.*, *93*, 5021–5036.
- Gargett, A. E., P. J. Hendricks, T. B. Sanford, T. R. Osborn and A. J. Williams III. 1981. A composite spectrum of vertical shear in the upper ocean. *J. Phys. Oceanogr.*, *11*, 1258–1271.
- Gargett, A. E., T. R. Osborn and P. R. Nasmyth. 1984. Local isotropy and the decay of turbulence in a stratified fluid. *J. Fluid Mech.*, *144*, 231–280.
- Garrett, C. 1990. The role of secondary circulation in boundary mixing. *J. Geophys. Res.*, *95*, 3181–3188.
- . 1991. Marginal mixing theories. *Atmos.-Ocean.*, *29*, 313–339.
- Gayen, B. and S. Sarkar. 2011. Boundary mixing by density overturns in an internal tidal beam. *Geophys. Res. Lett.*, *38*, L14608, doi:10.1029/2011GL048135.
- Gerkema, T. and H. van Haren. 2007. Internal tides and energy fluxes over Great Meteor Seamount. *Ocean Sci.*, *3*, 441–449.
- Gotoh, T. and D. Fukayama. 2001. Pressure spectrum in homogeneous turbulence. *Phys. Rev. Lett.*, *86*, 3775–3778.
- Gregg, M. C. 1989. Scaling turbulent dissipation in the thermocline. *J. Geophys. Res.*, *94*, 9686–9698.
- Hosegood, P., J. Bonnin and H. van Haren. 2004. Solibore-induced sediment resuspension in the Faeroe-Shetland Channel. *Geophys. Res. Lett.*, *31*, L09301, doi:10.1029/2004GL019544.
- Klymak, *et al.* 2006. An estimate of tidal energy lost to turbulence at the Hawaiian Ridge. *J. Phys. Oceanogr.*, *36*, 1148–1164.
- Klymak, J., S. Legg and R. Pinkel. 2010. A simple parameterization of turbulent tidal mixing near supercritical topography. *J. Phys. Oceanogr.*, *40*, 2059–2074.
- Klymak, J. M. and J. N. Moum. 2003. Internal solitary waves of elevation advancing on a shoaling shelf. *Geophys. Res. Lett.*, *30*, 2045, doi:10.1029/2003GL017706.
- Klymak, J., R. Pinkel and L. Rainville. 2008. Direct breaking of the internal tide near topography: Kaena Ridge. *J. Phys. Oceanogr.*, *38*, 380–399.
- Levine, M. D. and T. J. Boyd. 2006. Tidally forced internal waves and overturns observed on a slope: results from HOME. *J. Phys. Oceanogr.*, *36*, 1184–1201.
- Munk, W. 1966. “Abyssal recipes.” *Deep-Sea Res.*, *13*, 707–730.
- Munk, W. and C. Wunsch. 1998. Abyssal recipes II: Energetics of tidal and wind mixing. *Deep-Sea Res.* I, *45*, 1977–2010.
- Nash, J. D., M. H. Alford, E. Kunze, K. Martini and S. Kelly. 2007. Hotspots of deep ocean mixing on the Oregon continental slope. *Geophys. Res. Lett.*, *34*, L01605, doi:10.1029/GL028170.
- Osborn, T. R. 1980. Estimates of the local rate of vertical diffusion from dissipation measurements. *J. Phys. Oceanogr.*, *10*, 83–89.
- Phillips, O. M., J.-H. Shyu and H. Salmun. 1986. An experiment on boundary mixing: mean circulation and transport rates. *J. Fluid Mech.*, *173*, 473–499.
- Slinn, D. N. and J. J. Riley. 1996. Turbulent mixing in the oceanic boundary layer caused by internal wave reflection from sloping terrain. *Dyn. Atmos. Oc.*, *24*, 51–62.
- Smith, W. H. F. and D. T. Sandwell. 1997. Global seafloor topography from satellite altimetry and ship depth soundings. *Science*, *277*, 1957–1962.
- Thorpe, S. A. 1977. Turbulence and mixing in a Scottish loch. *Phil. Trans. Roy. Soc. Lond. A*, *286*, 125–181.
- . 1987. Transitional phenomena and the development of turbulence in stratified fluids: a review. *J. Geophys. Res.*, *92*, 5231–5248.

- Trowbridge, J. H. and S. J. Lentz. 1991. Asymmetric behavior of an oceanic boundary layer over a sloping bottom. *J. Phys. Oceanogr.*, *21*, 1171–1185.
- van Haren, H. 2005. Details of stratification in a sloping bottom boundary layer of Great Meteor Seamount. *Geophys. Res. Lett.*, *32*, L07606, doi:10.1029/2004GL02298.
- van Haren, H. and L. Gostiaux. 2010. A deep-ocean Kelvin-Helmholtz billow train. *Geophys. Res. Lett.*, *37*, L03605, doi:10.1029/2009GL041890.
- van Haren, H., M. Laan, D.-J. Buijsman, L. Gostiaux, M. G. Smit and E. Keijzer. 2009. NIOZ3: independent temperature sensors sampling yearlong data at a rate of 1 Hz, *IEEE J. Ocean. Eng.*, *34*, 315–322.
- van Haren, H., L. R. M. Maas and T. Gerkema. 2010. Patchiness in internal tidal beams. *J. Mar. Res.*, *68*, 237–257.
- Weatherly, G. L. and P. J. Martin. 1978. On the structure and dynamics of the oceanic bottom boundary layer. *J. Phys. Oceanogr.*, *8*, 557–570.
- Webb, S. C., X. Zhang and W. Crawford. 1991. Infragravity waves in the deep ocean. *J. Geophys. Res.*, *96*, 2723–2736.

Received: 1 April, 2011; revised: 23 October, 2011.